Application of reference-modified density functional theory: Temperature and pressure dependences of solvation free energy

Tomonari Sumi*[1,2], Yutaka Maruyama[3], Ayori Mitsutake[4], Kenji Mochizuki[1], and Kenichiro Koga[1,2]

[1]Research Institute for Interdisciplinary Science, Okayama University, 3-1-1 Tsushima-Naka, Kita-ku, Okayama 700-8530, Japan

[2]Department of Chemistry, Faculty of Science, Okayama University, 3-1-1 Tsushima-Naka, Kita-ku, Okayama 700-8530, Japan

[3]Co-Design Team, FLAGSHIP 2020 Project, RIKEN Advanced Institute for Computational Science, 7-1-26, Minatojima-minami-machi, Kobe 650-0047, Japan

[4]Department of Physics, Keio University, 3-14-1 Hiyoshi, Kohoku-ku, Yokohama, Kanagawa 223–8522, Japan

E-mail: sumi@okayama-u.ac.jp

ABSTRACT

Recently, we proposed a reference-modified density functional theory (RMDFT) to calculate solvation free energy (SFE), in which a hard-sphere fluid was introduced as the reference system instead of an ideal molecular gas. Through the RMDFT, using an optimal diameter for the hard-sphere reference system, the values of the SFE calculated at room temperature and normal pressure were in good agreement with those for more than 500 small organic molecules in water as determined by experiments. In this study, we present an application of the RMDFT for calculating the temperature and pressure dependences of the SFE for solute molecules in water. We demonstrate that the RMDFT has high predictive ability for the

1

temperature and pressure dependences of the SFE for small solute molecules in water when the optimal reference hard-sphere diameter determined for each thermodynamic condition is used. We also apply the RMDFT to investigate the temperature and pressure dependences of the thermodynamic stability of an artificial small protein, chignolin, and discuss the mechanism of high-temperature and high-pressure unfolding of the protein.

Introduction

The solvation free energy (SFE) is critical in understanding the thermodynamic stability of systems involving protein folding, protein-ligand binding, and the phase partitioning of chemicals. A free-energy perturbation method and a thermodynamic integration method [1,2] based on molecular dynamics (MD) simulations are both widely applied to SFE calculation. These calculations of the SFE are theoretically exact [3-6], but are highly computationally demanding, because MD simulations must be performed for many intermediate states in the process of growing a solute molecule in solution. To avoid calculations with high computational costs, many theoretical developments for the efficient calculation of the SFE, e.g., the implicit solvent model [7-11], integral equation theory [12-23], density functional theory (DFT) [24-27], and an energy representation method based on MD simulation [28-31], have been proposed. Although these methods offer the efficient prediction of the SFE, the accuracy of most methods in computing the SFE has been assessed only in cases at room temperature and normal pressure. Only a few methods [10,11,23] have been tested regarding the effect of temperature on the SFE. However, the solubility of small hydrophobic molecules is known to decrease dramatically with increases in temperature of ~ 100 K [32].

Recently, we proposed a reference-modified density functional theory (RMDFT) to systematically develop a free-energy density functional model [33,34]. In this RMDFT, in order to derive the SFE functional of a solute molecule in water, a hard-sphere (HS) fluid was

introduced as the reference system instead of an ideal polyatomic molecular gas. The latter is commonly employed as the reference system in the interaction-site-model DFT of polyatomic molecular liquids [35-39]. The SFE functional derived from the RMDFT approach with the hard-sphere reference system improved the overestimation of the SFE originating from the hypernetted-chain (HNC) approximation. For a set of neutral amino acid side-chain analogues, as well as 504 small organic molecules, the values of the SFE calculated by the RMDFT agreed well with those obtained by experiments [33,34]. In comparison to the MD simulation-based methods for SFE calculation, the RMDFT approach has the major advantage of high computational efficiency, permitting determination of the SFE value within a few minutes for both small molecules and large complex molecules such as proteins.

In the present study, we assess the predictive ability of the RMDFT for the temperature and pressure dependences of the SFE for small solute molecules in water. In our previous work [33,34], we found that the value of SFE obtained by the RMDFT was sensitive to the diameter of the HS reference system. Thus, we determined the optimal diameter of the HS reference system for water at room temperature and normal pressure; the SFE values given by the RMDFT were therefore in good agreement with those determined experimentally for three typical hydrophobic solutes of methane, propane, and isobutane [33,34]. Similar to the case at room temperature and normal pressure, by using either experimental data or MD simulation data for the SFE of a certain small molecule in water, here we determine the optimal diameters of the HS reference system at several temperatures and normal pressure and also at several pressures and room temperature. Next, to assess the applicability of the RMDFT using the determined HS diameters, we apply the RMDFT to the other solute molecules and compare the results calculated by the RMDFT with the corresponding experimental and MD-simulation data.

This report is organized as follows. In the second section, a brief review of the RMDFT is provided. In the third section, the calculation details including the SFE calculation and the determination of temperature and pressure dependences of the optimal HS diameter are described. In the fourth section, the calculated temperature dependence of the SFE for xenon in water and pressure dependences for methane and benzene molecule in water are compared with those determined by experiments or MD simulations. In addition, the temperature and pressure dependences of the SFE determined by the RMDFT for the artificial small protein chignolin are presented. Finally, a summary of this study is given.

Theory

In this section, we briefly review the RMDFT as well as the final equations for the SFE of a polyatomic solute molecule in water. In classical density functional theory (DFT), the grand potential under an arbitrary external field is expressed as a functional of the density distribution function of liquids under the external field. If the external fields acting on each site of water molecules $\left\{ U_\lambda^{PR} \right\}$ arise from a polyatomic solute molecule immersed in water, the solvation free energy ΔG_{solv} — defined as the difference in the free energies between the solvated state in solution and the un-solvated state without the solute — is given by the difference in the grand potential between the inhomogeneous system under the external field and the homogeneous system, i.e., $\Delta G_{solv} = \Omega \left[\left\{ U_\lambda^{PR} \right\} \right] - \Omega \left[0 \right]$. The superscript "PR" in $\left\{ U_\lambda^{PR} \right\}$ indicates the Percus relation [40], which provides an exact relation between the site–site pair correlation functions for solute and solvent and the one-body site density distribution functions for solvent under the external field $\left\{ U_\lambda^{PR} \right\}$ [38].

The hypernetted-chain (HNC) approximation has been demonstrated to significantly overestimate the SFE of solute molecules not only in molecular liquids such as water [33,34] but

also in simple liquids such as the Lennard-Jones (LJ) liquid [41]. The SFE based on the HNC approximation can also be derived from the DFT. We adapt the DFT as follows. First, we assume that the density distribution function under an arbitrary external field is reproduced by the density distribution function provided by an ideal-gas (IG) reference system under an effective external field for the IG. Second, we apply the second-order density-functional Taylor series expansion approximation to the excess part of the intrinsic free energy functional, which is defined as the difference from that given by the IG reference system. Thus, the large overestimation of the SFE caused by the HNC approximation suggests slow convergence in this density-functional Taylor series expansion and necessary inclusion of the higher-order terms. Unlike the HNC approximation, we choose a HS fluid, instead of the IG, as the reference system for the solvent. Next, we assume that the density distribution function is reproduced by the HS reference system under an effective external field. We showed previously that the RMDFT yielded sufficiently rapid convergence in the density-functional Taylor series expansion of the newly introduced excess part of the intrinsic free energy functional [33,42]. That excess part is redefined as the difference from the HS reference system in order to remove the component that leads to slow convergence [42].

Now, we consider an inhomogeneous solvent consisting of rigid water molecules having P interaction sites under the external field $\left\{U_\lambda^{PR}\right\}$ where $\lambda = 1, 2, 3, \cdots, P$. According to the DFT based on the interaction-site model [35-39], the grand potential under the external field, $\Omega\left[\left\{U_\lambda^{PR}\right\}\right] = -(1/\beta)\ln\Xi\left[\left\{U_\lambda^{PR}\right\}\right]$, where $\Xi\left[\left\{U_\lambda^{PR}\right\}\right]$ is the grand canonical partition function and $1/\beta$ is Boltzmann's constant multiplied by the absolute temperature, $k_B T$, is given by

$$\Omega\left[\left\{U_\lambda^{PR}\right\}\right] = F\left[\left\{n_\lambda\right\}\right] + \sum_{a=1}^{P}\int d\mathbf{r}_1^a n_a\left(\mathbf{r}_1^a \middle| \left\{U_\lambda^{PR}\right\}\right)\left[U_a^{PR}\left(\mathbf{r}_1^a\right) - \mu_a\right]. \tag{1}$$

Here, the sum of the site chemical potentials, μ_a, in eq. (1) is equal to the chemical potential for the polyatomic molecular fluid,

$$\mu = \sum_{a=1}^{P} \mu_a \ .$$

(2)

$F\big[\{n_\lambda\}\big]$ in eq. (1) is the intrinsic free-energy functional. The excess part of $F\big[\{n_\lambda\}\big]$ is introduced as the difference from a multicomponent HS reference system:

$$F^{ex}\big[\{n_\lambda\}\big] = F\big[\{n_\lambda\}\big] - F_{HS}\big[\{n_\lambda\}\big],$$

(3)

where Eq. (4) is substituted into $F_{HS}\big[\{n_\lambda^{HS}\}\big]$.

$$n_\alpha^{HS}\big(\mathbf{r}\big|\{U_\lambda^{HS}\}\big) = n_\alpha\big(\mathbf{r}\big|\{U_\lambda^{PR}\}\big) \ . \qquad (\alpha = 1,\, 2,\, \cdots,\, P)$$

(4)

Equation (4) is the most important assumption in the RMDFT, giving the definition of the effective external field acting on each component of the HS reference system. By applying a second-order density-functional Taylor series expansion to $F^{ex}\big[\{n_\lambda\}\big]$, we obtain the final equation for the SFE:

$$
\begin{aligned}
\Delta G_{solv} &= \Omega\big[\{U_\lambda^{PR}\}\big] - \Omega[0] \\
&= -\frac{1}{\beta}\sum_{a=1}^{P}\int d\mathbf{r}_1^a\Big[n_a\big(\mathbf{r}_1^a\big|\{U_\lambda^{PR}\}\big) - n_0\Big] + \Delta F_{HS}^{ex}\big[\{n_\lambda\}\big] \\
&\quad -\sum_{a=1}^{P}\int d\mathbf{r}_1^a\left[\frac{\delta F_{HS}^{ex}\big[\{n_\lambda\}\big]}{\delta n_a\big(\mathbf{r}_1^a\big|\{U_\lambda^{PR}\}\big)}n_a\big(\mathbf{r}_1^a\big|\{U_\lambda^{PR}\}\big) - \mu_a^{exHS}n_0\right] \\
&\quad +\frac{n_0}{\beta}\sum_{a=1}^{P}\sum_{b=1}^{P}\int d\mathbf{r}_1^a d\mathbf{r}_1^b C_{ab}^{ex}\big(|\mathbf{r}_1^a - \mathbf{r}_1^b|\big)\Big[n_b\big(\mathbf{r}_1^b\big|\{U_\lambda^{PR}\}\big) - n_0\Big] \\
&\quad +\frac{1}{2\beta}\sum_{a=1}^{P}\sum_{b=1}^{P}\int d\mathbf{r}_1^a d\mathbf{r}_1^b C_{ab}^{ex}\big(|\mathbf{r}_1^a - \mathbf{r}_1^b|\big)\Big[n_a\big(\mathbf{r}_1^a\big|\{U_\lambda^{PR}\}\big) - n_0\Big]\Big[n_b\big(\mathbf{r}_1^b\big|\{U_\lambda^{PR}\}\big) - n_0\Big]
\end{aligned}
$$

(5)

where n_0 is the number density of solvent molecules and

$$\Delta F_{HS}^{ex}\big[\{n_\lambda\}\big] = F_{HS}^{ex}\big[\{n_\lambda\}\big] - \Delta F_{HS}^{ex}\big[\{n_0\}\big] \ ,$$

(6)

$$F_{HS}^{ex}\big[\{n_\lambda\}\big] = F_{HS}\big[\{n_\lambda\}\big] - F_{IG}\big[\{n_\lambda\}\big] \ ,$$

(7)

$$\mu_\alpha^{exHS} = \mu_\alpha^{HS} - \mu_\alpha^{IG} \ ,$$

(8)

$$C_{\alpha\beta}^{ex}\big(|\mathbf{r} - \mathbf{r}'|\big) = \overline{C}_{\alpha\beta}\big(|\mathbf{r} - \mathbf{r}'|\big) - C_{\alpha\beta}^{HS}\big(|\mathbf{r} - \mathbf{r}'|\big) \ ,$$

(9)

$$\overline{C}_{\alpha\beta}\left(\left|\mathbf{r}-\mathbf{r}'\right|\right) = C_{\alpha\beta}\left(\left|\mathbf{r}-\mathbf{r}'\right|\right) - C_{\alpha\beta}^{IM}\left(\left|\mathbf{r}-\mathbf{r}'\right|\right) , \tag{10}$$

$$C_{\alpha\beta}^{IM}\left(\left|\mathbf{r}-\mathbf{r}'\right|\right) = \delta\left(\left|\mathbf{r}-\mathbf{r}'\right|\right)/n_0 - \sigma_{\alpha\beta}^{-1}\left(\left|\mathbf{r}-\mathbf{r}'\right|\right)/n_0 , \tag{11}$$

and

$$\sigma_{\alpha\beta}\left(\left|\mathbf{r}-\mathbf{r}'\right|\right) = \delta_{\alpha\beta}\delta\left(\left|\mathbf{r}-\mathbf{r}'\right|\right) + \left(1-\delta_{\alpha\beta}\right)s_{\alpha\beta}\left(\left|\mathbf{r}-\mathbf{r}'\right|\right) . \tag{12}$$

In eq. (7), $F_{IG}\left[\{n_\lambda\}\right]$ is an intrinsic free energy functional for a multicomponent IG system. μ_α^{HS} and μ_α^{IG} in eq. (8) are the chemical potentials of component α for the multicomponent HS and IG systems, respectively. $C_{\alpha\beta}^{HS}\left(\left|\mathbf{r}-\mathbf{r}'\right|\right)$ in eq. (9) is a direct correlation function for the multicomponent HS reference system, while $C_{\alpha\beta}\left(\left|\mathbf{r}-\mathbf{r}'\right|\right)$ in eq. (10) is a direct correlation function defined by the reference-interaction-site model (RISM) or site–site Ornstein–Zernike (OZ) equation [43-45] given by

$$\hat{H}_{\alpha\beta}(k) = \sum_{a=1}^{P}\sum_{b=1}^{P}\hat{\sigma}_{\alpha a}(k)\hat{C}_{ab}(k)\hat{\sigma}_{b\beta}(k) + n_0\sum_{a=1}^{P}\sum_{b=1}^{P}\hat{\sigma}_{\alpha a}(k)\hat{C}_{ab}(k)\hat{h}_{b\beta}(k) . \tag{13}$$

$C_{\alpha\beta}^{IM}\left(\left|\mathbf{r}-\mathbf{r}'\right|\right)$ in eq. (11) is an intramolecular direct correlation function, as discussed by Chandler *et al.* [35] $\sigma_{\alpha\beta}\left(\left|\mathbf{r}-\mathbf{r}'\right|\right)$ in eq. (12) is the intramolecular correlation function, where $\delta(r)$ is the Dirac delta function, $\delta_{\alpha\beta}$ is the Kronecker delta, and $s_{\alpha\beta}\left(\left|\mathbf{r}-\mathbf{r}'\right|\right)$ in eq. (12) is the intramolecular bonding function $s_{\alpha\beta}(r) = \delta\left(r-L_{\alpha\beta}\right)/4\pi L_{\alpha\beta}^2$ with the bond length between sites α and β in the water molecule of $L_{\alpha\beta}$. In eq. (13), $\hat{H}_{\alpha\beta}(k)$, $\hat{C}_{\alpha\beta}(k)$, and $\hat{\sigma}_{\alpha\beta}(k)$ are the Fourier transforms of the pair correlation function $H_{\alpha\beta}(r)$, the direct correlation function $C_{\alpha\beta}(r)$, and the intramolecular correlation function $\sigma_{\alpha\beta}(r)$, respectively.

In the standard point-charge models of water such as the three-point transferable intermolecular potential (TIP3P) [46] and extended simple point-charge (SPC/E) model [47], the two sites for the hydrogen atoms are embedded in the LJ particle representing the oxygen

atom. In these water models, a one-component HS system is usable as the reference system for water. In this case, equation (5) is reduced to

$$
\begin{aligned}
\Delta G_{solv} = &-\frac{1}{\beta}\sum_{a=1}^{P}\int d\mathbf{r}_1^a\left[n_a\left(\mathbf{r}_1^a\left|\left\{U_\lambda^{PR}\right\}\right.\right)-n_0\right]+\Delta F_{HS}^{ex}\left[n_O\right]\\
&-\int d\mathbf{r}_1^O\left[\frac{\delta F_{HS}^{ex}\left[n_O\right]}{\delta n_O\left(\mathbf{r}_1^O\left|\left\{U_\lambda^{PR}\right\}\right.\right)}n_O\left(\mathbf{r}_1^O\left|\left\{U_\lambda^{PR}\right\}\right.\right)-\mu_O^{exHS}n_0\right]\\
&+\frac{n_0}{\beta}\sum_{a=1}^{P}\sum_{b=1}^{P}\int d\mathbf{r}_1^a d\mathbf{r}_1^b C_{ab}^{ex}\left(\left|\mathbf{r}_1^a-\mathbf{r}_1^b\right|\right)\left[n_b\left(\mathbf{r}_1^b\left|\left\{U_\lambda^{PR}\right\}\right.\right)-n_0\right]\\
&+\frac{1}{2\beta}\sum_{a=1}^{P}\sum_{b=1}^{P}\int d\mathbf{r}_1^a d\mathbf{r}_1^b C_{ab}^{ex}\left(\left|\mathbf{r}_1^a-\mathbf{r}_1^b\right|\right)\left[n_a\left(\mathbf{r}_1^a\left|\left\{U_\lambda^{PR}\right\}\right.\right)-n_0\right]\left[n_b\left(\mathbf{r}_1^b\left|\left\{U_\lambda^{PR}\right\}\right.\right)-n_0\right]
\end{aligned}
\tag{14}
$$

with

$$
C_{ab}^{ex}\left(\left|\mathbf{r}-\mathbf{r}'\right|\right)=\begin{cases}\bar{C}_{OO}\left(\left|\mathbf{r}-\mathbf{r}'\right|\right)-C_{OO}^{HS}\left(\left|\mathbf{r}-\mathbf{r}'\right|\right) & (\alpha=\beta=O)\\[2mm]\bar{C}_{\alpha\beta}\left(\left|\mathbf{r}-\mathbf{r}'\right|\right) & (\text{otherwise})\end{cases}.
\tag{15}
$$

where O indicates the oxygen site. $\Delta F_{HS}^{ex}\left[n_O\right]$, $\delta F_{HS}^{ex}\left[n_O\right]\big/\delta n_O\left(\mathbf{r}_1^O\left|\left\{U_\lambda^{PR}\right\}\right.\right)$, μ_O^{exHS} in eq. (14), and $C_{OO}^{HS}\left(\left|\mathbf{r}-\mathbf{r}'\right|\right)$ in eq. (15) correspond to those of the reference HS fluid having a HS diameter d_{HS} and the number density same as n_0. Since we can use an arbitrary excess intrinsic free-energy functional model for the reference system in the RMDFT, several options for the excess intrinsic free-energy function model used for the reference HS fluid is available [48-51].

Calculation method

Computational details

In this study, we apply an effective-density approximation (EDA) [51] to prepare the excess intrinsic free-energy functional for the HS reference system, $F_{HS}^{ex}\left[n\right]$, which is needed in eq. (14). The RMDFT calculation of the SFE using the EDA functional obtained from the EDA as $F_{HS}^{ex}\left[n\right]$ is relatively easy, because the EDA functional is much simpler than the functional

model provided by the fundamental measure theory (FMT) [48] or the modified versions of it [49,50]. In our previous study, the EDA functional was demonstrated to predict ΔG_{solv} well for various small solute molecules in water [33,34]. Equation (14), rewritten using the EDA functional, is shown in the Supporting Information (SI).

To determine the site-density distribution functions $n_\alpha\left(\mathbf{r}\left|\left\{U_\lambda^{PR}\right\}\right.\right)$ in eq. (14), we apply the three-dimensional reference-interaction-site-model (3D-RISM) theory [45,52]. We employ a partially linearized HNC (PLHNC) equation [52], called the Kovalenko–Hirata (KH) equation [45], as the closure relations for both the 1D-RISM equation for bulk water and the 3D-RISM equation for solute–solvent systems. The details of the 1D-RISM and 3D-RISM calculations are shown in the SI. To model water in these RISM calculations, we use the TIP3P model with an additional LJ parameter for the hydrogen sites ($d_H = 0.4$ Å and $\varepsilon_H = 0.046$ kcal/mol) [46,53]. We employ the optimized potentials for liquid simulations using all atoms (OPLS-AA) parameter for both methane and benzene, and use the LJ parameter for xenon ($d_{Xe} = 3.975$ Å and $\varepsilon_{Xe}/k_B = 214.7$) from the literature [32]. The solute–solvent cross parameters are deduced from the Lorentz–Berthelot mixing rules, $d_{ij} = \left(d_{ii} + d_{jj}\right)/2$ and $\varepsilon_{ij} = \sqrt{\varepsilon_{ii}\varepsilon_{jj}}$, commonly introduced as the solute–solvent combination rule in the RISM calculations. The number densities of water used in the calculations at several temperatures along the isobar of 1 bar and at several pressures along the isotherm of 298 K (Tables 1 and 2) are obtained from the experimental data [54] and the MD simulation results [55,56], respectively. For comparison with the computational results for ΔG_{solv} obtained by the RMDFT, we also calculate the values of ΔG_{solv} using the Singer–Chandler-like (SC-like) 3D-RISM-KH function [45,52]. The 3D-RISM integral equations are solved using a grid of 256^3 points in a cubic cell with a size of 64 Å³, as in our previous study [33,34]. The grid spacing of 0.25 Å is sufficient to calculate ΔG_{solv} for chignolin without significant numerical errors.

In our previous study, we determined the optimal diameter of the HS reference system as $d_{HS} = 2.88$ Å at room temperature and under normal pressure ($T = 298$ K, $P = 1$ bar); the ΔG_{solv} values obtained by the RMDFT were in good agreement with the experimental values of ΔG_{solv} for three small hydrophobic solutes of methane, propane, and isobutane [33,34] (see Fig. 2 in the references [33,34]). In these calculations, we used 0.01 Å and 4096 as the grid spacing and the number of grids, respectively, to solve the 1D-RISM and EDA integral equations. However, in the present study, we employ 0.00125 Å and 32768 as the grid spacing and number of grids, respectively, for the 1D-RISM and EDA calculations, because a detailed adjustment of the HS diameter d_{HS} is required to determine d_{HS} for each thermodynamic state. If we use the fine grid spacing of 0.00125 Å in the EDA calculation for the reference HS fluid, we find a slight shortening of d_{HS} by 0.005 Å at the normal condition (298 K and 1 bar). The d_{HS} dependences of ΔG_{solv} for these three solutes obtained by the RMDFT calculation with the fine grid spacing of 0.00125 Å are compared in the SI with those obtained by the RMDFT with the grid spacing of 0.01 Å. Based on these results, we determine $d_{HS} = 2.8750$ Å as optimal at the normal condition.

Temperature and pressure dependences of the optimal diameter of the HS reference system

In the present study, we determine the appropriate d_{HS} values at several temperatures along the isobar of 1 bar and at several pressures along the isotherm of 298 K to ensure that the values of ΔG_{solv} obtained by the RMDFT are in good agreement with those determined by either experiments or MD simulations. For the temperature dependence along the 1-bar isobar, we employ the experimental values of ΔG_{solv} for methane [57] at each temperature T listed in Table 1 as the reference data. Even at the normal condition (298 K and 1 bar), the values of ΔG_{solv} for methane obtained by the RMDFT with the newly determined optimal HS diameter $d_{HS} =$

2.8750 Å deviate by ~0.3 kcal/mol from the experimental data. Thus, we focus on the temperature dependence of the difference of ΔG_{solv} between the standard state ($T = 298$ K and $P = 1$ bar) and each temperature, i.e., $\Delta G_{solv}^* = \Delta G_{solv} - \Delta G_{solv}(298 \text{ K})$, to determine the temperature dependence of the optimal HS diameter d_{HS}. The asterisk after any physical quantity indicates the difference of that quantity from the standard thermodynamic state at room temperature and normal pressure. To assess the applicability of the RMDFT to the temperature dependence of ΔG_{solv}, we also apply the RMDFT with the optimal HS diameters to the calculation of ΔG_{solv} for xenon, and then compare the computed values of ΔG_{solv} to the experimental data.

Similar to determining the temperature dependence of d_{HS} along the 1-bar isobar, we also determine the pressure dependence of d_{HS} along the isotherm of 298 K by fitting the values of $\Delta G_{solv}^* = \Delta G_{solv} - \Delta G_{solv}(1 \text{ bar})$ that are obtained by the RMDFT for a water molecule in water to that by MD simulations [58]. The excess chemical potential of water, i.e., ΔG_{solv}, the number density of water n_0 obtained from MD simulations [55,56], and the determined d_{HS} are listed in Table 2.

Table 1. The solvation free energy ΔG_{solv} experimentally determined for methane in water [57], experimental number density of water n_0 [54], and optimal diameter of the HS reference system d_{HS}, at several temperatures along the isobar of 1 bar. These ΔG_{solv} and n_0 values are used to determine d_{HS}.

T (K)	ΔG_{solv} (kcal/mol)	n_0 (Å^{-3})	d_{HS} (Å)
273	1.561	0.033422	2.88250
298	1.982	0.033329	2.87500
325	2.351	0.032994	2.87125
350	2.598	0.032526	2.87000
373	2.744	0.031924	2.87250

Table 2. The solvation free energy ΔG_{solv} for a water molecule in water provided by MD simulation [58], the number density of water n_0 determined by MD simulation [55,56], and the optimal diameter of the HS reference system d_{HS}, at several pressures along the isotherm of 298 K. These ΔG_{solv} and n_0 values are used to determine d_{HS}.

P (bar)	ΔG_{solv} (kcal/mol)	n_0 (Å^{-3})	d_{HS} (Å)
1	-6.13	0.033357	2.87500
2000	-5.32	0.035927	2.83250
4000	-4.52	0.037795	2.80375
6000	-3.87	0.039265	2.78375
8000	-3.15	0.040483	2.76750

Application of the RMDFT calculation to an artificial small protein chignolin

To further apply the RMDFT to the temperature and pressure dependences of ΔG_{solv}, we perform the RMDFT calculation of ΔG_{solv} on nine conformations of chignolin, a small artificial protein comprising 10 amino acids with the sequence GYDPETGTWG [59]. Previous studies have demonstrated that chignolin has native and misfolded states [60-64]. The native and misfolded structures are hairpin-like, with a common turn structure from Asp3 to Glu5, although these have different hydrogen bonding patterns. The nine conformations used in this

study were generated by performing an isobaric–isothermal (*NPT*) MD simulation in an aqueous solution for 6 μs at 298 K and 1 bar, where the Amber99SB parameter and the TIP3P model were employed for chignolin and water, respectively [61]. The nine conformations, including the native and misfolded conformations, are the same as those used in our previous study [33,34].

Results and discussion

Temperature dependences of the solvation free energy and optimal HS diameter

Figure 1 (a) shows a comparison between the experimental values of ΔG_{solv} for methane along the isobar of 1 bar [57] and the computational values of ΔG_{solv} obtained by the RMDFT using the d_{HS} determined at each temperature. These values of ΔG_{solv} for methane monotonically increase as the temperature increases from 273 K to 373 K. The positive value of ΔG_{solv} and the positive temperature dependence are characteristic of hydrophobic hydration. The RMDFT reproduces the temperature dependence, but slightly underestimates the value of ΔG_{solv} at each temperature. The underestimation is attributed to the optimal HS diameter being determined as $d_{HS} = 2.875$ Å at 298 K and 1 bar based on experimental data for methane as well as for propane and isobutane (see the SI). However, in Fig. 1 (b), we can confirm that the temperature dependences of the experimental and theoretical $\Delta G_{solv}^{*} = \Delta G_{solv} - \Delta G_{solv}(298 \text{ K})$ agree well with each other. On the other hand, not only the values of ΔG_{solv} but also the temperature dependence of ΔG_{solv}^{*}, as calculated by the SC-like RISM-KH function [45,52], deviate from the experimental values. This function overestimates the temperature variation of ΔG_{solv}. To examine the electrostatic contribution to ΔG_{solv} for methane, we also calculated ΔG_{solv} for methane without any electric charge, i.e., the nonpolar contribution. Because the electrostatic contribution to ΔG_{solv} (–0.01607 kcal/mol at 298 K) is

very small, ΔG_{solv} and ΔG_{solv}^* without the electric charges almost overlap with the values shown in Figs. 1 (a) and (b), respectively. These results indicate that almost all of ΔG_{solv} for methane arises from the nonpolar contribution. In Fig. 1 (c), the temperature dependence of the optimal HS diameter d_{HS} is non-monotonic with the minimum at the temperature of ~350 K.
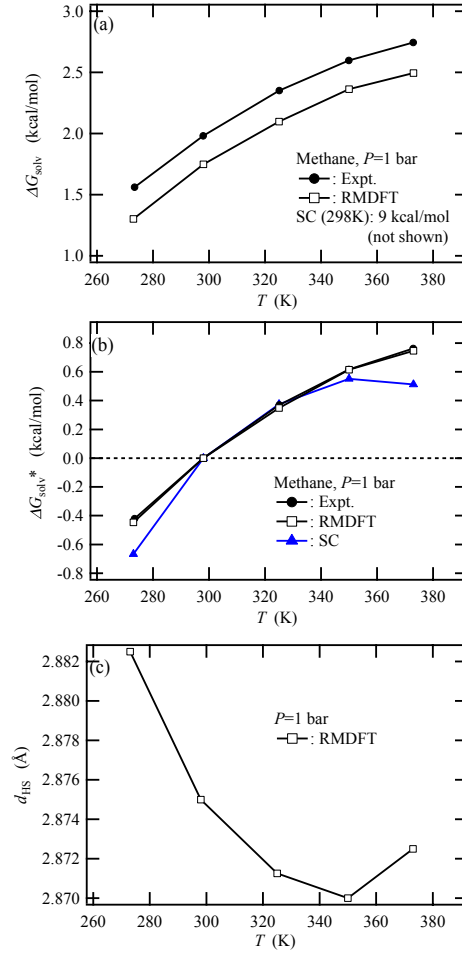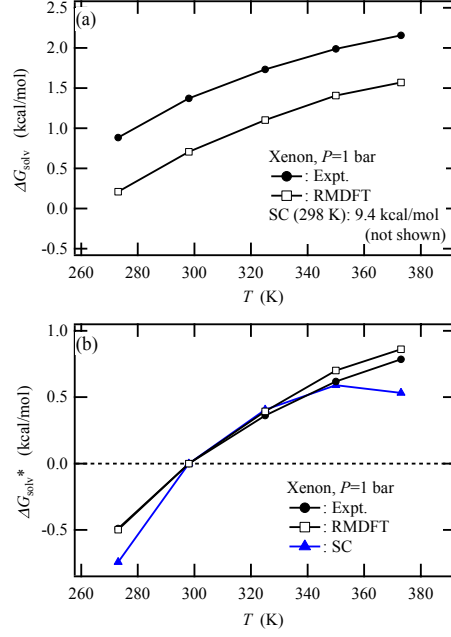

Figure 1. Temperature dependences of (a) the solvation free energy ΔG_{solv} for methane, (b) the difference of the ΔG_{solv} values between each temperature and 298 K,

$\Delta G_{solv}^* = \Delta G_{solv} - \Delta G_{solv}(298\ \text{K})$, and (c) the optimal HS diameter d_{HS} determined at each temperature, along the 1-bar isobar. In (a) and (b), the experimental values for methane [57] are shown as solid circles. The theoretical values obtained by the RMDFT and the SC-like RISM-KH function [45,52] are shown as open squares and blue solid triangles, respectively.

14

To confirm the validity of the determined d_{HS} values, we apply the RMDFT to xenon in water. Figure 2 (a) shows the values of ΔG_{solv} for xenon along the 1-bar isobar from the experiments [57] and by the RMDFT using the d_{HS} values listed in Table 1. The temperature dependence of $\Delta G_{solv}^{*} = \Delta G_{solv} - \Delta G_{solv}(298\ \text{K})$ is also shown in Fig. 2(b), with a similar tendency to that in Fig. 1. The RMDFT slightly underestimates the values of ΔG_{solv} for xenon. However, the SC function [45,52] yields ΔG_{solv} = 9.4 kcal/mol at 298 K, which is a significant overestimation. ΔG_{solv} for xenon is experimentally known to be smaller than ΔG_{solv} for methane at a given temperature (see Fig. 1(a) and Fig. 2(a)), although xenon is larger than methane. The RMDFT provides the correct tendency, while the SC function [45,52], for instance at 298 K, gives a positive of 9.4 kcal/mol for xenon and 9.0 kcal/mol for methane. The overestimation of ΔG_{solv} caused by this function, especially for large solutes, is attributed to the drawback of the HNC approximation for the cavity-formation free energy [17]. From Fig. 2 (b), we confirm that the values of ΔG_{solv} obtained by the RMDFT agree well with those from the experiments, while those of the SC function deviate from the experimental values. These results demonstrate that the RMDFT with the d_{HS} value can accurately predict the temperature dependence of ΔG_{solv} for small hydrophobic solutes.
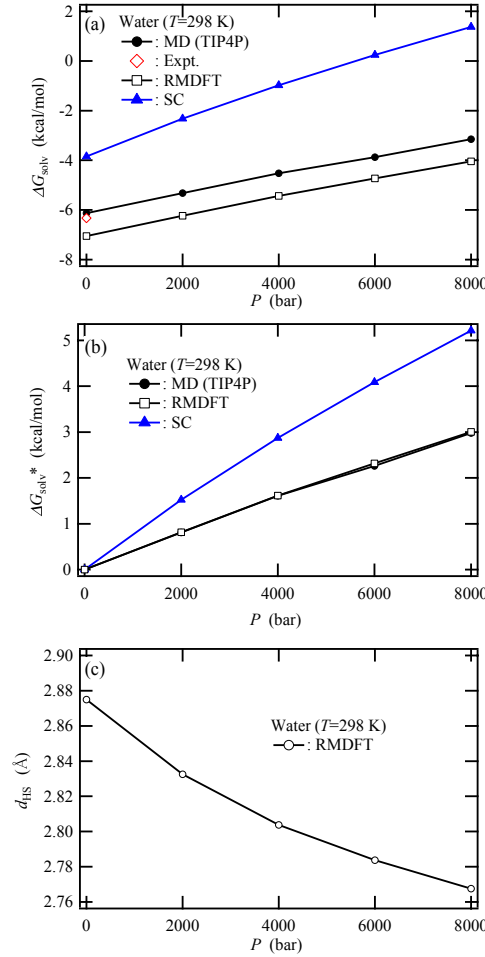
Figure 2. Temperature dependences of (a) the solvation free energy ΔG_{solv} for xenon and (b) the difference of the ΔG_{solv} values between each temperature and 298 K, ΔG_{solv}^*, along the 1-bar isobar. In (a) and (b), the experimental values for xenon [57] are shown as solid circles. The theoretical values obtained by the RMDFT with d_{HS} and by the SC function [45,52] are shown as open squares and blue solid triangles, respectively.

Pressure dependences of the solvation free energy and optimal HS diameter

Figure 3 (a) shows the values of ΔG_{solv} for a water molecule in water along the isotherm of 298 K, as obtained by the MD simulation with the TIP4P model of water [58], RMDFT with d_{HS}, and SC function [45,52]. The value of ΔG_{solv} for water monotonically increases with increasing pressure. The pressure derivative of ΔG_{solv} at constant temperature corresponds to the excess partial molar volume (PMV) of the solute. The RMDFT with d_{HS} underestimates ΔG_{solv} for water, but reproduces the pressure dependence of $\Delta G_{solv}^* = \Delta G_{solv} - \Delta G_{solv}\left(1 \text{ bar}\right)$ well, as shown in Fig. 3 (b). This result indicates that the excess PMV of water is reproduced with high precision. Meanwhile, the SC function [45,52] overestimates both the values of ΔG_{solv} and

the pressure derivative of ΔG_{solv}^{*}. In Fig. 3 (c), we find that d_{HS} for water monotonically decreases with increasing pressure.

Figure 3. Pressure dependences of (a) the solvation free energy ΔG_{solv} for a water molecule in water, (b) the difference of ΔG_{solv} from 1 bar, ΔG_{solv}^{*}, and (c) d_{HS} along the isotherm of 298 K. In (a) and (b), the values of ΔG_{solv} provided by the MD simulation [58] are shown as solid circles. The theoretical values obtained by the RMDFT and by the SC function [45,52] are shown as open squares and blue solid triangles, respectively. In (a), the red open diamond indicates an experimental value for the excess chemical potential of water [58].

To confirm the validity of the obtained $d_{\scriptscriptstyle HS}$ values, we apply the RMDFT to calculate ΔG_{solv} for methane and benzene in water along the isotherm of 298 K. In Fig. 4 (a), the RMDFT slightly underestimates the values of ΔG_{solv} for methane compared to the experimental data [65], while the values of $\Delta G_{solv}^* = \Delta G_{solv} - \Delta G_{solv}(1\ \text{bar})$ obtained by the RMDFT agree well with the experimental values as seen in Fig. 4 (b). However, the SC function overestimates both the values of ΔG_{solv} and the pressure derivative of ΔG_{solv}. In Fig. 4 (c), we find that the RMDFT slightly underestimates the values of ΔG_{solv} for benzene compared to those obtained by the MD simulation [58]. The value of ΔG_{solv} by the RMDFT is relatively closer to that by the experiment for benzene under 1 bar [58], as indicated as an red open diamond in Fig. 4 (c). In Fig. 4 (d), we observe that the RMDFT with $d_{\scriptscriptstyle HS}$ reproduces the values of ΔG_{solv}^* for benzene, while the SC function overestimates both the values of ΔG_{solv} (e.g., 17 kcal/mol at 1 bar) and the pressure derivative of ΔG_{solv}^*. These results demonstrate that the RMDFT with $d_{\scriptscriptstyle HS}$ can reproduce the pressure dependence of ΔG_{solv} for small solute molecules with high precision.
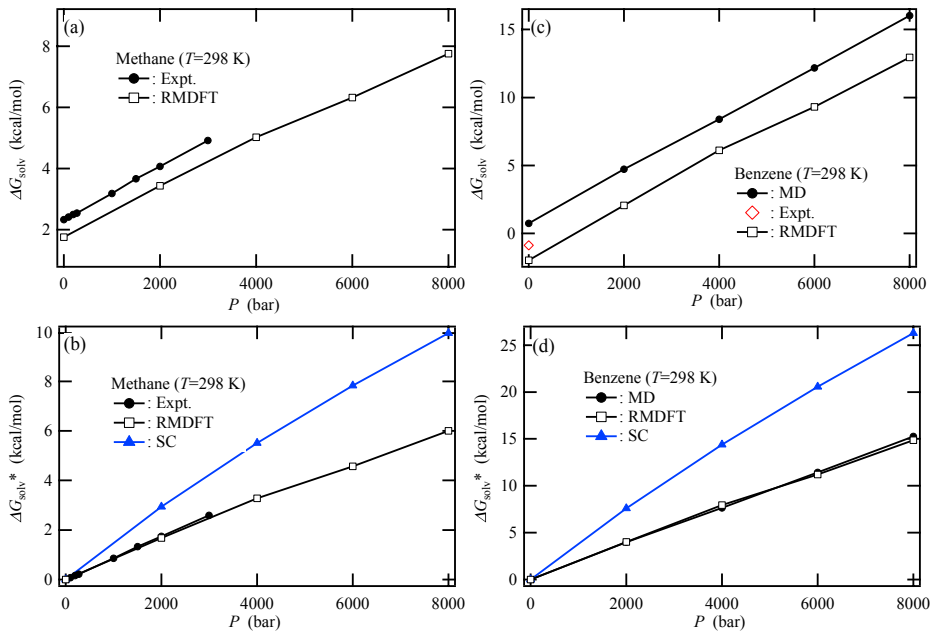
Figure 4. Pressure dependences of the solvation free energy ΔG_{solv} for (a) methane and (c) benzene; pressure dependences of the difference in ΔG_{solv} between each pressure and 1 bar, ΔG_{solv}^{*}, for (b) methane and (d) benzene, along the isotherm of 298 K. The solid circles in (a) and (b) indicate the experimental values for methane [65] and the solid circles in (c) and (d) indicate the values obtained by the MD simulation for benzene [58]. The open squares and blue solid triangles indicate the theoretical values obtained by the RMDFT and SC function [45,52], respectively. In (c), the red open diamond indicates the experimental value for the excess chemical potential of benzene in water [58].

Solvent effects on the stability of chignolin at room temperature and normal pressure

To further apply the RMDFT to the temperature and pressure effects on ΔG_{solv}, we calculate ΔG_{solv} for nine conformations of chignolin [59], as used in our previous study (Conf. 1 to 9 in this study respectively correspond to Conf. A to I in our previous study [33,34]). The solvation free energy ΔG_{solv}, the structure energy E_i^{st}, and the effective energy given by $E_i^{\mathrm{eff}} = E_i^{\mathrm{st}} + \Delta G_i$, for the nine conformations are shown in Figs. 5 (a), (b), and (c), respectively. Here, the effective energy E_i^{eff} is introduced to examine the change in the relative stability of chignolin with each conformation in water. It is noted that changes in the effective energy E_i^{eff} due to conformation changes are different from changes in the free energy; thus, we cannot discuss the absolute value of the appearance probability of each conformation based on the value of E_i^{eff}. However, we believe that we can use E_i^{eff} to discuss changes in the relative stability among the different conformations caused by changes in temperature and pressure. In Fig. 5 (a), the electrostatic contribution, $\Delta G_i^{\mathrm{elec}} = \Delta G_i - \Delta G_i^{\mathrm{np}}$, where ΔG_i^{np} is the nonpolar contribution calculated without all the electric charges on chignolin, is also shown. The nine

conformations are numbered in decreasing order of ΔG_i (Fig. 5 (a)), which also roughly corresponds to the increasing order of the structure energy E_i^{st} of chignolin, shown in Fig. 5 (b). Based on the root mean square deviation (RMSD) from the native structure (Conf. 1) in water as determined by nuclear magnetic resonance (NMR) (PDB ID code 1UAO), we find that Confs. 1 and 3 correspond to the native and misfolded structure, respectively. In terms of the radius of gyration R_g (Fig. 5 (d)), Confs. 8 and 9 are extended structures.

From Fig. 5 (a), we find that the extended structures have low SFE; the main contribution to ΔG_i for Conf. i is attributable to the electrostatic contribution ΔG_i^{elec}. Thus, the unfolded conformations are stabilized in water by the electrostatic interactions between the protein and water. Figure 5 (b) shows that the structure energy of chignolin E_i^{st} overall increases as the conformation number increases, except that E_i^{st} for the misfolded conformation of Conf. 3 is lower than E_i^{st} for Conf. 2. Therefore, the compactness of the native Conf. 1 can be attributed to its structure energy E_i^{st}. Figure 5 (c) shows that the effective energy E_i^{eff} tends to increase with increasing conformation number. Confs. 1 and 3 have comparable stabilities with effective energies lower than those of the other conformations. The balance between E_i^{st} and ΔG_i yields the relative stability of each conformation in water at room temperature and normal pressure. In fact, although the increase in E_i^{st} and the decrease in ΔG_i as the conformation transforms from native to extended states are largely canceled out, the increase in E_i^{st} tends to overcome the decrease in ΔG_i, and thus the effective energy E_i^{eff} for the native Conf. 1 becomes lower that for the unfolding conformations [66]. Such a balance also relates to the relative stability of the native and misfolded structures (Confs. 1 and 3, respectively): E_i^{st} for Conf. 1 is lower than that for Conf. 3, whereas ΔG_i for Conf. 3 is lower than that for Conf. 1. Therefore, Confs. 1 and 3 have

nearly equal stabilities. As found in comparing Confs. 1 and 3, different mechanisms for the stabilization of the protein in water are suggested (in preparation by Maruyama and Mitsutake).

Figure 5 (e) shows the excess PMV, V_i^{ex}, determined using the Kirkwood integral of the density distribution function with respect to the oxygen site of water:

$$V^{ex} = -\int d\mathbf{r}_1 \left[n_O\left(\mathbf{r}_1 \middle| \left\{ U_\lambda^{PR} \right\} \right) \middle/ n_0 - 1 \right].\qquad(16)$$

Here, the density distribution function $n_O\left(\mathbf{r}_1 \middle| \left\{ U_\lambda^{PR} \right\} \right)$ in eq. (16) is calculated using the 3D-RISM integral equation. The nonpolar contribution to V_i^{ex} is provided by eq. (16), where $n_O\left(\mathbf{r}_1 \middle| \left\{ U_\lambda^{PR} \right\} \right)$ is calculated using the 3D-RISM equation omitting all the electric charges on chignolin. We find that the electrostatic interaction between the protein and water reduces V_i^{ex}, especially in extended conformations such as Confs. 8 and 9. Figure 5 (f) is discussed in detail later on.
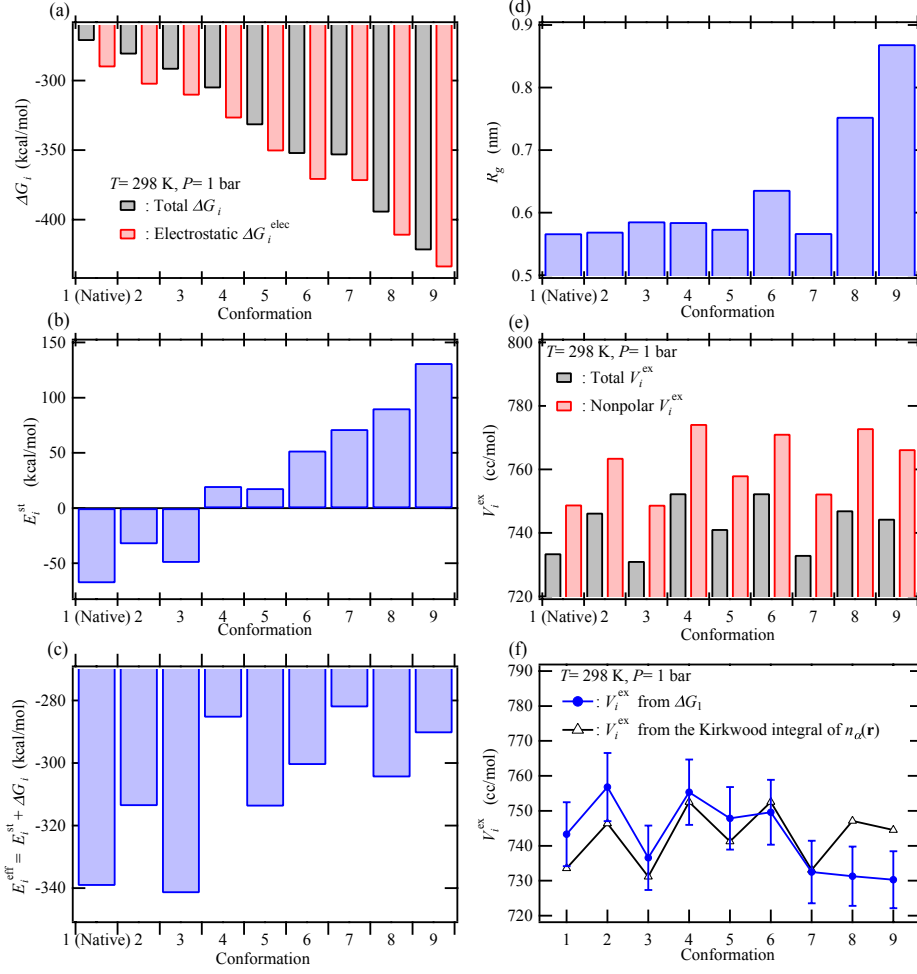
Figure 5. (a) The solvation free energy ΔG_i and the electrostatic contribution ΔG_i^{elec}, (b) the structure energy E_i^{st}, (c) the effective energy given by $E_i^{\text{eff}} = E_i^{\text{st}} + \Delta G_i$, (d) the radius of gyration R_g, (e) the excess partial molar volume V_i^{ex} and the nonpolar contribution, and (f) a comparison between the values of V_i^{ex} calculated using two different methods described below, for the nine conformations of chignolin at 298 K and 1 bar. In Fig. 5 (e), V_i^{ex} obtained by eq. (16) is shown together with the nonpolar contribution to V_i^{ex}, wherein the solvent density distribution function in eq. (16) is obtained by the 3D-RIDM calculation omitting all the electrostatic charges of chignolin. In Fig. 5 (f), V_i^{ex} obtained by the Kirkwood integral of eq. (16) (shown in Fig. 5(e)) is compared with V_i^{ex} determined as the coefficient V_i^0 in $\Delta G_i = \Delta G_i^0 + V_i^0 (p - p_0)$ (eq. (19)). The error bars in Fig. 5 (f) indicate the standard

deviations upon the fitting by eq. (19) to the pressure dependence of ΔG_i. In these figures, Conf. 1 is the native structure and the conformation number increases in decreasing order of ΔG_i.

Temperature effects on change in ΔG_{solv} by the unfolding of chignolin

Figure 6 (a) shows the temperature dependences of the solvation free energy $\Delta G_1/k_B T$, the nonpolar contribution $\Delta G_1^{\mathrm{np}}/k_B T$, and the electrostatic contribution $\Delta G_1^{\mathrm{elec}}/k_B T$, for chignolin with the native Conf. 1 along the isobar of 1 bar. The nonpolar contribution $\Delta G_1^{\mathrm{np}}/k_B T$ is positive and the absolute value of $\Delta G_1^{\mathrm{np}}/k_B T$ is smaller than that of the electrostatic contribution $\Delta G_1^{\mathrm{elec}}/k_B T$. Furthermore, we find that the increase in $\Delta G_1^{\mathrm{elec}}/k_B T$ with increasing temperature is significantly larger than the increase in $\Delta G_1^{\mathrm{np}}/k_B T$ for a large amphipathic molecule such as chignolin. We also calculate the excess solvation enthalpy and entropy from the following equations:[67]

$$h_1^{\mathrm{ex}} = \left[\partial\left(\Delta G_1/T \right)/\partial\left(1/T \right) \right]_p + k_{\mathrm{B}} T^2 \alpha_p, \tag{17a}$$

$$s_1^{\mathrm{ex}} = -\left(\partial \Delta G_1/\partial T \right)_p + k_{\mathrm{B}} T \alpha_p, \tag{17b}$$

where α_p is the thermal expansion coefficient of water at 1 bar. By applying these equations to the nonpolar contribution ΔG_1^{np} and electrostatic contribution $\Delta G_1^{\mathrm{elec}}$, we can obtain the corresponding excess solvation enthalpies h_1^{np} and h_1^{elec} (Fig. 6 (b)) and entropies s_1^{np} and s_1^{elec} (Fig. 6 (c)). In Fig. 6 (b), we find that $h_1^{\mathrm{ex}}/k_B T$ increases as temperature increases, and that the increase in $h_1^{\mathrm{ex}}/k_B T$ contributes to the increase in $\Delta G_1/k_B T$ with increasing temperature. The electrostatic contribution $h_1^{\mathrm{elec}}/k_B T$, defined by $h_1^{\mathrm{ex}}/k_B T - h_1^{\mathrm{np}}/k_B T$, has a positive slope with respect to temperature. Therefore, $h_1^{\mathrm{elec}}/k_B T$ contributes to the increase in

$\Delta G_1 / k_B T$ with the increase in temperature. In Fig. 6 (c), we find that s_1^{ex} / k_B has negative values and a positive slope with temperature, that is, the excess solvation entropy term, $-s_1^{ex} / k_B$, in $\Delta G_1 / k_B T = h_1^{ex} / k_B T - s_1^{ex} / k_B$, decreases with temperature. However, the electrostatic part $-s_1^{elec} / k_B$ (defined by $-s_1^{ex} / k_B + s_1^{np} / k_B$) increases with temperature, as does $h_1^{elec} / k_B T$.

Figure 6 (d) shows the values of the effective energy $E_i^{eff} / k_B T$ for each conformation at 298 K and 373 K. The values of $E_i^{eff} / k_B T$ for the unfolded conformations are higher than that for the native Conf. 1 and the differences of $E_i^{eff} / k_B T$ between Conf. 1 and these unfolded conformations remain significantly large even at 373 K, although the differences are smaller at 373 K than at 298 K. Thus, the relative stability of the unfolded conformations to that of Conf. 1 increases as temperature increases. It is well known that the free energy for the unfolded state is more stabilized by the conformation entropy of the protein than that for the native state is [68]; thus, even for differences in the effective energy values between the native and denatured conformations of tens of $k_B T$, most of those differences are canceled out in the free energy by the conformation entropy [68]. A model for the conformation entropy of polypeptides [69] was proposed as follows:

$$-S_C / k_B = -N_r \left[\ln(9) + 1.7 \right],$$
(18)

where N_r is the number of residues in the polypeptides. For ten amino acid residues, as for chignolin, $-S_C / k_B$ is estimated as –38.97. The differences of $E_i^{eff} / k_B T$ between the native and unfolded conformations—~30–80—are mostly compensated by the conformation entropy contribution of –38.97. However, none of the unfolded conformations investigated in the present study, except for Conf. 5, has a sum of $E_i^{eff} / k_B T$ and $-S_C / k_B$ less than that for Conf. 1, even at 373 K, although some other conformations may have such sums. These arguments

imply that, even if the difference of the effective energy between Conf. 1 and the arbitrary

denatured Conf. i, i.e., $\Delta E_i^{\text{eff}} / k_{\text{B}}T = \left[E_i^{\text{eff}} - E_1^{\text{eff}} \right] / k_{\text{B}}T$, is positive, an appropriate decrease in

$\Delta E_i^{\text{eff}} / k_{\text{B}}T$ by increasing the temperature yields a negative value for the free energy

difference between the native and denatured states, $\Delta F / k_{\text{B}}T = \left(F_D - F_N \right) / k_{\text{B}}T$, where F_N and

F_D are the free energy values for the native state and the denatured state, respectively.

As for chignolin, the temperature dependence of the molar fraction of the native state f_N was

extensively examined by Honda *et al.* [59]. Based on their experimental results, we estimate

$\Delta F / k_{\text{B}}T$ using $\Delta F / k_{\text{B}}T = -\ln \left[\left(1 - f_N \right) / f_N \right]$. The values of f_N at 298 K and 373 K are

obtained as 0.6 and 0.1, respectively; thus, we can determine $\Delta F / k_{\text{B}}T$ to be 0.4 at 298 K and

−2.2 at 373 K. Therefore, the increase in temperature from 298 K to 373 K causes the relative

thermodynamic stabilization of the denatured state compared to the native state by

approximately −2.6 (= −0.4 − 2.2) in the free energy difference $\Delta F / k_{\text{B}}T$ (see schematic free

energy profiles based on the experimental data, shown in the SI). Thus, to obtain insight into

the mechanism of high-temperature protein unfolding, it is useful to examine whether changes

in $\Delta E_i^{\text{eff}} / k_{\text{B}}T$ by increasing the temperature stabilize the unfolded conformations to a degree

comparable to the stabilization provided by the free energy change $\Delta F / k_{\text{B}}T$ in unfolding.
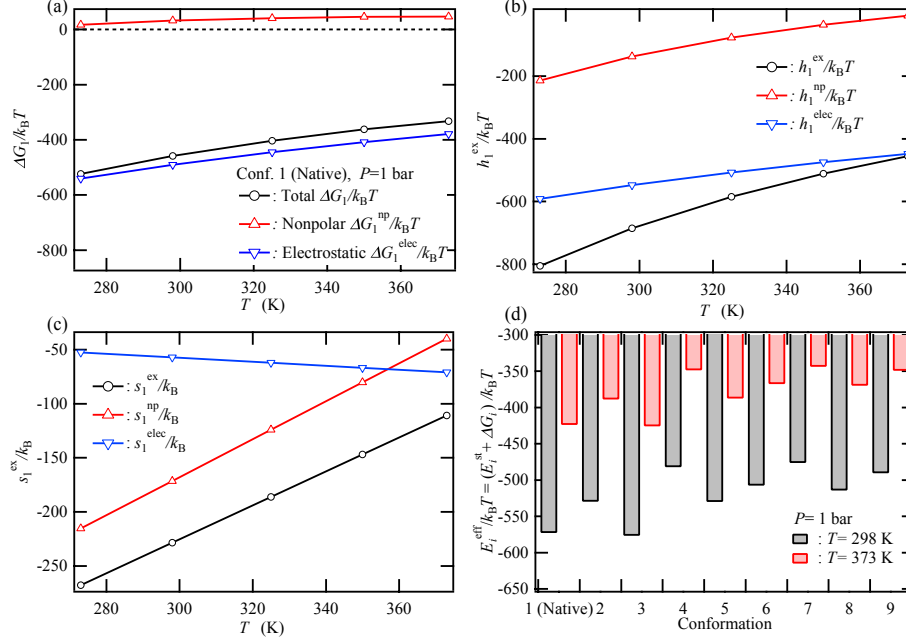
Figure 6. (a) Temperature dependences of the SFE for chignolin with the native structure (Conf. 1) $\Delta G_1/k_BT$, the nonpolar contribution $\Delta G_1^{np}/k_BT$ calculated without all the electric charges on chignolin, and the electrostatic contribution defined by

$\Delta G_1^{elec}/k_BT = \left[\Delta G_1 - \Delta G_1^{np}\right]/k_BT$, along the isobar of 1 bar. (b) Temperature dependences of

the corresponding excess solvation enthalpies, h_1^{ex}/k_BT, h_1^{np}/k_BT, and h_1^{elec}/k_BT, and of (c)

the corresponding excess solvation entropies, s_1^{ex}/k_B, s_1^{np}/k_B, and s_1^{elec}/k_B. (d) The effective

energy $E_i^{eff}/k_BT = \left[E_i^{st} - \Delta G_i\right]/k_BT$ for each conformation at temperatures of 298 K and 373

K.

For investigating the temperature dependence of the relative stability between Confs. 1 and i,

we show $\left(\Delta E_i^{eff}/k_BT\right)^* = \Delta E_i^{eff}/k_BT - \left(\Delta E_i^{eff}/k_BT\right)_{T=298\,K}$ as a function of temperature along the

1-bar isobar (Fig. 7 (a)). By definition, the values of $\left(\Delta E_i^{eff}/k_BT\right)^*$ for all the conformations

are zero at the standard state (298 K and 1 bar), as seen in Fig. 7 (a). The change in the

26

effective energy $\left(\Delta E_i^{\mathrm{eff}}/k_{\mathrm{B}}T\right)^*$ due to conformational change from Confs. 1 to i, except that to the misfolded conformation (Conf. 3), is monotonically decreased as the temperature increases, indicating that these unfolded conformations are relatively stabilized by increasing temperature. The decrease in $\left(\Delta E_i^{\mathrm{eff}}/k_{\mathrm{B}}T\right)^*$ of approximately -5 to -15 with temperatures increasing from 298 K to 373 K contributes to the high-temperature denaturation of chignolin. The exceptional behavior observed for the misfolded conformation (Conf. 3) is discussed later.

In Figs. 7 (b) and (c), each contribution to $\left(\Delta E_i^{\mathrm{eff}}/k_{\mathrm{B}}T\right)^*$ caused by the structure energy, $\left(\Delta E_i^{\mathrm{st}}/k_{\mathrm{B}}T\right)^*$, and by the SFE, $\left(\Delta\Delta G_i/k_{\mathrm{B}}T\right)^*$, is shown as a function of temperature, respectively. The change in the structure energy from Confs. 1 to i, ΔE_i^{st}, is large and positive; thus, $\left(\Delta E_i^{\mathrm{st}}/k_{\mathrm{B}}T\right)^*$ as well as ΔE_i^{st} divided by $k_{\mathrm{B}}T$ should decrease with increasing temperature (Fig. 7 (b)). However, the change in the SFE from Confs. 1 to i $\Delta\Delta G_i$ and $\left(\Delta\Delta G_i/k_{\mathrm{B}}T\right)^*$ both increase with increasing temperature (Fig. 7 (c)). The increase in $\left(\Delta\Delta G_i/k_{\mathrm{B}}T\right)^*$ indicates that the solvent effect stabilizes Conf. 1 relative to the unfolded conformations at higher temperatures, thereby suppressing high-temperature unfolding. The decrease in $\left(\Delta E_i^{\mathrm{st}}/k_{\mathrm{B}}T\right)^*$ and the increase in $\left(\Delta\Delta G_i/k_{\mathrm{B}}T\right)^*$ are mostly canceled by each other; the decrease in $\left(\Delta E_i^{\mathrm{st}}/k_{\mathrm{B}}T\right)^*$ slightly overcomes the increase in $\left(\Delta\Delta G_i/k_{\mathrm{B}}T\right)^*$. Therefore, the stabilization of the unfolded conformations relative to Conf. 1 is increased by the increase in temperature. These observations suggest that, in addition to the larger stabilization for the unfolded conformations than for the native Conf. 1 from the conformation entropy, the decrease in $\left(\Delta E_i^{\mathrm{st}}/k_{\mathrm{B}}T\right)^*$ by increasing temperature, i.e., the thermal fluctuation effect on protein conformation, is important in stabilizing denatured conformations at high temperatures.

As for the misfolded conformation, $E_3^{\mathrm{eff}}/k_{\mathrm{B}}T$ for Conf. 3 remains slightly lower than that for Conf. 1 even at 373 K (see Fig. 6 (d)). The value of $\left(\Delta E_i^{\mathrm{eff}}/k_{\mathrm{B}}T\right)^*$ only for Conf. 3 increases as temperature increases (see Fig. 7 (a)), indicating that the relative stability of Conf. 3 to Conf. 1 is increased by increasing temperature. In the previous paragraph, we noted that ΔE_i^{st} and $\Delta\Delta G_i$ were mostly canceled out, except the former contributed slightly more to $\Delta E_i^{\mathrm{eff}}$. All conformations except for Conf. 3 have this tendency, i.e., $\left|\Delta E_i^{\mathrm{st}}\right|>\left|\Delta\Delta G_i\right|$, even for increasing temperature. However, in the case of Conf. 3, $\Delta\Delta G_i$ overcomes ΔE_i^{st} at all temperatures; that is, $\left|\Delta E_i^{\mathrm{st}}\right|<\left|\Delta\Delta G_i\right|$. Even though E_i^{st} for Conf. 1 is lower than that for Conf. 3, Conf. 3 is slightly more stabilized than Conf. 1; this is because the solvation effect on the stabilization of Conf. 3 is larger than that of Conf. 1 at all temperatures.

To investigate why $\left(\Delta\Delta G_i/k_{\mathrm{B}}T\right)^*$ increases with increasing temperature, we divide the quantity into the nonpolar contribution $\left(\Delta\Delta G_i^{\mathrm{np}}/k_{\mathrm{B}}T\right)^*$ and the electrostatic contribution $\left(\Delta\Delta G_i^{\mathrm{elec}}/k_{\mathrm{B}}T\right)^*$, defined by $\left(\Delta\Delta G_i^{\mathrm{elec}}/k_{\mathrm{B}}T\right)^*=\left(\Delta\Delta G_i/k_{\mathrm{B}}T\right)^*-\left(\Delta\Delta G_i^{\mathrm{np}}/k_{\mathrm{B}}T\right)^*$. Hydrophobic interactions between small solutes such as methane become stronger by increasing the temperature [for instance, Ref. [70]]. The increase in the nonpolar contribution $\left(\Delta\Delta G_i^{\mathrm{np}}/k_{\mathrm{B}}T\right)^*$ shown in Fig. 7 (d) can be interpreted based on the temperature dependence of hydrophobic interactions. However, the electrostatic contribution $\left(\Delta\Delta G_i^{\mathrm{elec}}/k_{\mathrm{B}}T\right)^*$ shown in Fig. 7 (e) yields a contribution to the increase in $\left(\Delta\Delta G_i/k_{\mathrm{B}}T\right)^*$ of approximately ten times that from the nonpolar contribution $\left(\Delta\Delta G_i^{\mathrm{np}}/k_{\mathrm{B}}T\right)^*$. The larger increase in $\left(\Delta\Delta G_i^{\mathrm{elec}}/k_{\mathrm{B}}T\right)^*$ can be interpreted as follows: the increase in the electrostatic contribution $\Delta G_i^{\mathrm{elec}}/k_{\mathrm{B}}T$ with increasing temperature is generally larger than that in the nonpolar contribution $\Delta G_i^{\mathrm{np}}/k_{\mathrm{B}}T$, as

seen in Fig. 6 (a), and the unfolded conformations have larger electrostatic contributions $\Delta G_i^{\mathrm{elec}}/k_{\mathrm{B}}T$ than the native Conf. 1 does because they have larger solvent-accessible surface areas, thus resulting in larger increases in $\left(\Delta\Delta G_i^{\mathrm{elec}}/k_{\mathrm{B}}T\right)^*$ than in $\left(\Delta\Delta G_i^{\mathrm{np}}/k_{\mathrm{B}}T\right)^*$.
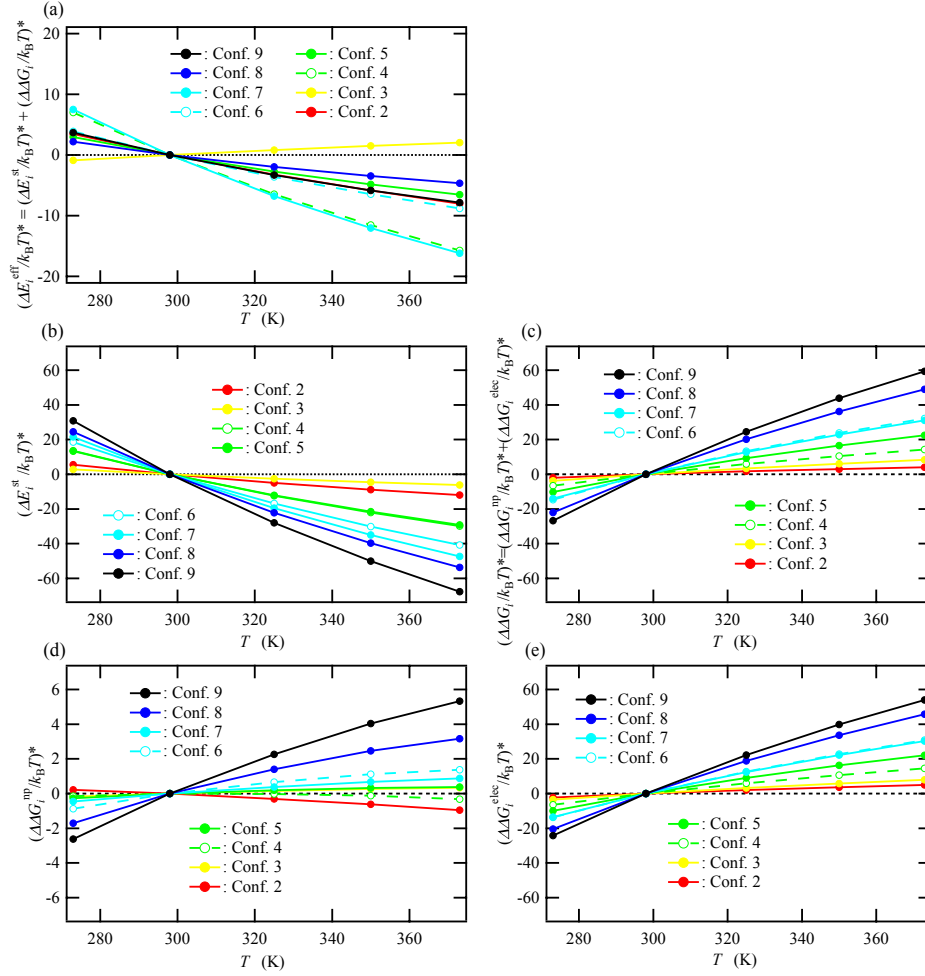
Figure 7. Temperature dependences of (a) the difference of the effective energy between the native Conf. 1 and Conf. i, $\left(\Delta E_i^{\mathrm{eff}}/k_{\mathrm{B}}T\right)^* = \left(\Delta E_i^{\mathrm{st}}/k_{\mathrm{B}}T\right)^* + \left(\Delta\Delta G_i/k_{\mathrm{B}}T\right)^*$, (b) the difference of the structure energy between Confs. 1 and i, $\left(\Delta E_i^{\mathrm{st}}/k_{\mathrm{B}}T\right)^*$, (c) the difference of the SFE between Confs. 1 and i, $\left(\Delta\Delta G_i/k_{\mathrm{B}}T\right)^*$, (d) the nonpolar contribution to $\left(\Delta\Delta G_i/k_{\mathrm{B}}T\right)^*$, $\left(\Delta\Delta G_i^{\mathrm{np}}/k_{\mathrm{B}}T\right)^*$, and (e) the electrostatic contribution to $\left(\Delta\Delta G_i/k_{\mathrm{B}}T\right)^*$, $\left(\Delta\Delta G_i^{\mathrm{elec}}/k_{\mathrm{B}}T\right)^*$, along

the isobar of 1 bar. In these figures, the asterisk added to the physical quantities indicates that these quantities are shown as the difference between the quantity at each temperature and that at 298 K, e.g., $\left(\Delta E_i^{\mathrm{eff}}/k_{\mathrm{B}}T\right)^{*} = \Delta E_i^{\mathrm{eff}}/k_{\mathrm{B}}T - \left(\Delta E_i^{\mathrm{eff}}/k_{\mathrm{B}}T\right)_{T=298\,\mathrm{K}}$, etc.

Pressure effects on change in ΔG_{solv} ***by the unfolding of chignolin***

Figure 8 (a) shows the pressure dependences of the SFE for Conf. 1, $\Delta G_1/k_{\mathrm{B}}T$, the nonpolar contribution, $\Delta G_1^{\mathrm{np}}/k_{\mathrm{B}}T$, and the electrostatic contribution, $\Delta G_1^{\mathrm{elec}}/k_{\mathrm{B}}T$, along the isotherm of 298 K. The nonpolar contribution $\Delta G_1^{\mathrm{np}}/k_{\mathrm{B}}T$ is positive and increases with increasing pressure, whereas the electrostatic contribution $\Delta G_1^{\mathrm{elec}}/k_{\mathrm{B}}T$ has a large negative value and conversely decreases with increasing pressure. The excess PMV V_i^{ex} is determined by the pressure dependence of ΔG_i using

$$\Delta G_i = \Delta G_i^{0} + V_i^{0}\left(p - p_0\right) \tag{19}$$

where $p_0 = 1$ bar. The coefficient V_i^{0} gives V_i^{ex} at 1 bar. The values of V_i^{ex} obtained by eq. (19) and by the Kirkwood integral (eq. (16)) are shown in Fig. 5 (f). The values of V_i^{ex} obtained by eq. (19) are almost comparable with those obtained by eq. (16) except for the extended conformations (Confs. 8 and 9), while the difference between them is attributed to the lack of the bridge function correction on the Kirkwood integral (eq. (16)). The density distribution function of water obtained by the 3D-RISM/KH integral equation—which is needed in eq. (16)—includes no bridge function correction. The increase or decrease in V_i^{ex} obtained by eq. (19) upon increasing the conformation number almost agrees with that by eq. (16), except for the change between Confs. 7 and 8. V_i^{ex} by eq. (19) gradually decreases with increasing conformation number; this indicates that the unfolded conformations are relatively stabilized by increasing pressure.

Figure 8 (b) shows the values of $E_i^{\mathrm{eff}}/k_{\mathrm{B}}T$ for each conformation at pressures of 1 bar and

8000 bar. The values of $E_i^{\mathrm{eff}}/k_{\mathrm{B}}T$ for the unfolded conformations are higher than that for

Conf. 1 and the differences of $E_i^{\mathrm{eff}}/k_{\mathrm{B}}T$ from Conf. 1 are ~50–80, even at 8000 bar. As

discussed in the temperature dependence of $E_i^{\mathrm{eff}}/k_{\mathrm{B}}T$ (Fig. 6 (d)), the large positive values of

the difference in the effective energy between the native and denatured conformations

$\Delta E_i^{\mathrm{eff}}/k_{\mathrm{B}}T$ are mostly compensated by the conformation-entropy contribution. Therefore, we

focus on whether the change in $\Delta E_i^{\mathrm{eff}}/k_{\mathrm{B}}T$ with increasing pressure yields a decrease in

$\Delta E_i^{\mathrm{eff}}/k_{\mathrm{B}}T$ comparable with an experimentally determined change in the free energy

$\Delta F/k_{\mathrm{B}}T$ due to the unfolding of chignolin. Based on the experimental results by Honda *et al.*

[59], $\Delta F/k_{\mathrm{B}}T$ at 298 K is estimated at ~0.4. This result shows that the free energy of the

denatured state is higher than that of the native state by ~0.4 $k_{\mathrm{B}}T$. Therefore, at least 0.4 $k_{\mathrm{B}}T$ is

required to render the denatured state more stable than the native state at room temperature

and normal pressure (298 K and 1 bar) (see the SI). Assuming that the fraction for the native

state at 298 K and 8000 bar is, e.g., $f_N = 0.3$, we can estimate $\Delta F/k_{\mathrm{B}}T = -\ln\left[\left(1 - f_N\right)/f_N\right]$ as

−0.85. Therefore, the relative stabilization in the free energy for the denatured state by

increasing the pressure is estimated at approximately −1.25 (= −0.4 − 0.85) in units of $k_{\mathrm{B}}T$. We

use this value as a reference one of the free energy change upon the high-pressure

denaturation of chignolin.
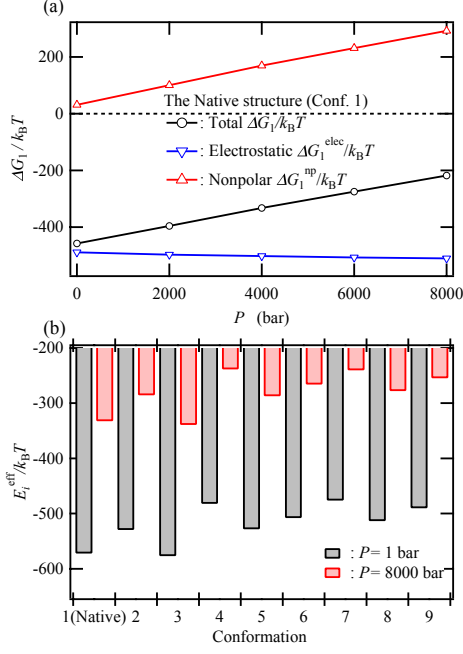
Figure 8. (a) Pressure dependences of the SFE for chignolin with the native Conf. 1 $\Delta G_1/k_{\mathrm{B}}T$, the nonpolar contribution $\Delta G_1^{\mathrm{np}}/k_{\mathrm{B}}T$, and the electrostatic contribution $\Delta G_1^{\mathrm{elec}}/k_{\mathrm{B}}T$ along the isotherm of 298 K. (b) The effective energy for each conformation defined by $E_i^{\mathrm{eff}}/k_{\mathrm{B}}T = \left[E_i^{\mathrm{st}} - \Delta G_i \right]/k_{\mathrm{B}}T$ at pressures of 1 bar and 8000 bar.

To investigate the pressure dependence of the relative stability between Confs. 1 and i, we show $\left(\Delta E_i^{\mathrm{eff}}/k_{\mathrm{B}}T\right)^* = \Delta E_i^{\mathrm{eff}}/k_{\mathrm{B}}T - \left(\Delta E_i^{\mathrm{eff}}/k_{\mathrm{B}}T\right)_{P=1\ \mathrm{bar}}$ as a function of pressure along the isotherm of 298 K (Fig. 9 (a)). $\left(\Delta E_i^{\mathrm{eff}}/k_{\mathrm{B}}T\right)^*$ is equivalent to $\left(\Delta\Delta G_i/k_{\mathrm{B}}T\right)^*$ because the contribution from the structure energy $\Delta E_i^{\mathrm{st}}/k_{\mathrm{B}}T$ is constant at any pressure. In Fig. 9 (a), $\left(\Delta\Delta G_i/k_{\mathrm{B}}T\right)^*$ for conformation group A, including Confs. 2, 4, 5, and 6, increases with increasing pressure, while $\left(\Delta\Delta G_i/k_{\mathrm{B}}T\right)^*$ for conformation group B, including Confs. 3, 7, 8, and 9, decreases. This implies that the relative stability of groups A and B is respectively decreased and increased by increasing pressure and that the relative stabilization for group B

is caused by $\left(\Delta\Delta G_i/k_BT\right)^*$, the solvent effect. The change in the relative stability for group B by approximately -2 to -4 k_BT, as seen in Fig. 9 (a), may be the driving force of the pressure-induced denaturation. The pressure derivative of $\Delta\Delta G_i$ at constant temperature provides changes in the excess PMV by changes in conformation from Confs. 1 to i, $\Delta V_i = V_i^{ex} - V_1^{ex}$. Therefore, groups A and B have positive and negative values of ΔV_i, respectively. If the pressure is increased to 8000 bar or higher, Conf. 1 changes into conformations of group B.

To clarify the mechanism of the relative stabilization for group B at high pressures, we divide $\left(\Delta\Delta G_i/k_BT\right)^*$ into the nonpolar contribution $\left(\Delta\Delta G_i^{np}/k_BT\right)^*$ and the electrostatic contribution $\left(\Delta\Delta G_i^{elec}/k_BT\right)^*$. The nonpolar contribution $\left(\Delta\Delta G_i^{np}/k_BT\right)^*$ shown in Fig. 9 (b) monotonically increases as pressure increases except for Confs. 3 and 7, while the electrostatic contribution $\left(\Delta\Delta G_i^{elec}/k_BT\right)^*$ for all the unfolded conformations decreases with increasing pressure (see Fig. 9 (c)). In Fig. 9 (b), the conformations with the highest two and lowest two values of $\left(\Delta\Delta G_i^{np}/k_BT\right)^*$ are Confs. 4 and 6 and Confs. 3 and 7, respectively, and the former and latter are destabilized and stabilized with increasing pressure, respectively, as seen in Fig. 9 (a).

In Fig. 9 (c), the lowest two and highest two values of $\left(\Delta\Delta G_i^{elec}/k_BT\right)^*$ are given by Confs. 8 and 9 and Confs. 2 and 3, respectively. The former has a large value of R_g, while the latter has a small value of R_g (see Fig. 5 (d)). This observation indicates that the extended conformations with larger R_g—which are solvated by more water molecules—gain larger stabilization from the electrostatic contribution $\left(\Delta\Delta G_i^{elec}/k_BT\right)^*$. Now we focus on Confs. 3 and 8, both of which yield decreases in $\left(\Delta\Delta G_i/k_BT\right)^*$, i.e., negative values of ΔV_i. The misfolded Conf. 3 is compact with a small R_g comparable to that of Conf. 1, and thus has a smaller electrostatic

contribution $\left(\Delta\Delta G_i^{\mathrm{elec}}/k_{\mathrm{B}}T\right)^*$ than the other extended conformations, while the increase in the nonpolar contribution $\left(\Delta\Delta G_i^{\mathrm{np}}/k_{\mathrm{B}}T\right)^*$ with increasing pressure is significantly suppressed by the compactness of Conf. 3. As a result, $\left(\Delta\Delta G_i/k_{\mathrm{B}}T\right)^*$ for Conf. 3 decreases with increasing pressure, even though the decreasing rate in $\left(\Delta\Delta G_i^{\mathrm{elec}}/k_{\mathrm{B}}T\right)^*$ with the increase in pressure is small. Sufficiently compact denatured conformations, such as Conf. 3, were proposed by Harano and Kinoshita as the fundamental high-pressure conformations [71]. Meanwhile, Conf. 8 is a typical extended conformation unlike Conf. 3; it has a large value of R_g and exhibits a large decrease in the electrostatic contribution $\left(\Delta\Delta G_i^{\mathrm{elec}}/k_{\mathrm{B}}T\right)^*$ upon increasing pressure. Although the increase in the nonpolar contribution $\left(\Delta\Delta G_i^{\mathrm{np}}/k_{\mathrm{B}}T\right)^*$ for Conf. 8 is larger than that for Conf. 3, the larger decrease in the electrostatic contribution $\left(\Delta\Delta G_i^{\mathrm{elec}}/k_{\mathrm{B}}T\right)^*$ for Conf. 8 overcomes the increase in $\left(\Delta\Delta G_i^{\mathrm{np}}/k_{\mathrm{B}}T\right)^*$. As a result, the pressure-induced stabilization of the extended conformation is caused by electrostatic interactions and/or hydrogen bonds between the protein and water. The extended conformations, whose large solvent-accessible surface areas enhance the electrostatic contributions $\left(\Delta\Delta G_i^{\mathrm{elec}}/k_{\mathrm{B}}T\right)^*$, are critical for the pressure-induced denaturation of proteins. Furthermore, as seen in Fig. 9 (a), the existence of unfolded conformations such as Confs. 2, 4, 5, and 6 with intermediate values of R_g—destabilized by increasing pressure—suggests the existence of high transition states suppressing pressure-induced unfolding.
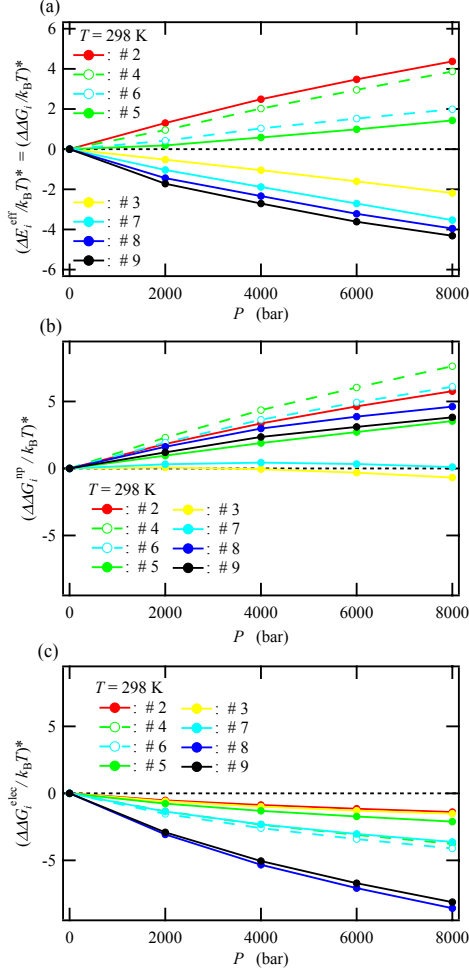
Figure 9. Pressure dependences of (a) the difference of the SFE between Confs. 1 and i $\left(\Delta\Delta G_i/k_{\mathrm{B}}T\right)^{*}$, (b) the nonpolar contribution, $\left(\Delta\Delta G_i^{\mathrm{np}}/k_{\mathrm{B}}T\right)^{*}$, and (c) the electrostatic contribution, $\left(\Delta\Delta G_i^{\mathrm{elec}}/k_{\mathrm{B}}T\right)^{*}$, along the isotherm of 298 K. It is noted that $\left(\Delta\Delta G_i/k_{\mathrm{B}}T\right)^{*}$ is equivalent to $\left(\Delta E_i^{\mathrm{eff}}/k_{\mathrm{B}}T\right)^{*} = \left(\Delta E_i^{\mathrm{st}}/k_{\mathrm{B}}T\right)^{*} + \left(\Delta\Delta G_i/k_{\mathrm{B}}T\right)^{*}$, because $\Delta E_i^{\mathrm{st}}/k_{\mathrm{B}}T$ is constant at any pressure.

Conclusion

In this study, we presented an application of the reference-modified density functional theory (RMDFT) to calculate the temperature and pressure dependences of the SFE for several small and large solute molecules in water. In this approach, we introduced a HS fluid as the reference system instead of a polyatomic molecular IG. Since the SFE calculated by the

RMDFT was sensitive to the diameter of the HS in the reference system, we determined the temperature dependence of the HS diameter under 1 bar such that the SFE values of methane in water by the RMDFT quantitatively agreed with those obtained experimentally. Similarly, we determined the pressure dependence of the HS diameter along the isotherm of 298 K such that the SFE values of a water molecule in water by the RMDFT quantitatively agreed with those determined by MD simulations. To assess the reliability of the RMDFT for estimating the temperature and pressure dependences of the SFE, we demonstrated the following: the SFE values calculated by the RMDFT at several temperatures under 1 bar agreed well with those experimentally determined for xenon in water; those calculated at several pressures at 298 K agreed with those experimentally determined for methane in water, as well as those obtained by MD simulations for a benzene molecule in water.

As a further application of the RMDFT to a large solute molecule, we investigated the temperature dependence of the SFE for chignolin, an artificial small protein [59], immersed in water with nine different conformations. The SFE for the native Conf. 1 $\Delta G_1 / k_B T$ monotonically increased as the temperature increased along the isobar of 1 bar, as seen in the temperature dependence of the SFE for the hydrophobic solutes, methane and xenon. $\Delta G_1 / k_B T$ was divided into the nonpolar contribution, $\Delta G_1^{np} / k_B T$, and the electrostatic contribution, $\Delta G_1^{elec} / k_B T$. The former was calculated without all the electric charges on the protein and the latter was given by $\Delta G_1^{elec} / k_B T = \left[\Delta G_1 - \Delta G_1^{np} \right] / k_B T$. The nonpolar contribution $\Delta G_1^{np} / k_B T$ had a positive small value and slightly increased with increasing temperature. The electrostatic contribution $\Delta G_1^{elec} / k_B T$ had a large negative value, i.e., provided the main contribution to $\Delta G_1 / k_B T$, and the increase in $\Delta G_1^{elec} / k_B T$ with increasing temperature was larger than that in the nonpolar contribution $\Delta G_1^{np} / k_B T$.

The values of the effective energy divided by $k_{\mathrm{B}}T$, $E_i^{\mathrm{eff}}/k_{\mathrm{B}}T = \left(E_i^{\mathrm{st}} + \Delta G_i\right)/k_{\mathrm{B}}T$, for the unfolded conformations except for the misfolded Conf. 3 were all higher than that for Conf. 1 even at the high temperature of 373 K. However, the differences of the effective energy between Confs. 1 and i divided by $k_{\mathrm{B}}T$, $\Delta E_i^{\mathrm{eff}}/k_{\mathrm{B}}T = \left(\Delta E_i^{\mathrm{eff}} - \Delta E_1^{\mathrm{eff}}\right)/k_{\mathrm{B}}T$, monotonically decreased as temperature increased, except for Conf. 3. The decrease in $\left(\Delta E_i^{\mathrm{eff}}/k_{\mathrm{B}}T\right)^*$ (or $\Delta E_i^{\mathrm{eff}}/k_{\mathrm{B}}T$) with increasing temperature provided a sufficiently large contribution to decrease the free energy for the unfolded state by $-2.6\ k_{\mathrm{B}}T$ [59], estimated based on the experiment results (see the SI). The decomposition of $\left(\Delta E_i^{\mathrm{eff}}/k_{\mathrm{B}}T\right)^*$ into the structure energy contribution $\left(\Delta E_i^{\mathrm{st}}/k_{\mathrm{B}}T\right)^*$ and the SFE contribution $\left(\Delta\Delta G_i/k_{\mathrm{B}}T\right)^*$ indicated that the relative stability of the unfolded conformations at high temperatures was attributable to the decrease in $\left(\Delta E_i^{\mathrm{st}}/k_{\mathrm{B}}T\right)^*$, interpreted as the thermal fluctuation effect on the protein conformation. Interestingly, $\left(\Delta\Delta G_i/k_{\mathrm{B}}T\right)^*$ provided greater stabilization to the native structure than to the unfolded conformations at high temperatures; thus, the solvent effect by $\left(\Delta\Delta G_i/k_{\mathrm{B}}T\right)^*$ suppressed high-temperature unfolding.

We also investigated the pressure dependence of the SFE for chignolin with nine conformations along the isotherm of 298 K. The SFE for Conf. 1 $\Delta G_1/k_{\mathrm{B}}T$ was increased by increasing pressure, while the electrostatic contribution $\Delta G_1^{\mathrm{elec}}/k_{\mathrm{B}}T$ was conversely decreased by increasing pressure. Thus, the increase in $\Delta G_1/k_{\mathrm{B}}T$ was attributable to increasing the nonpolar contribution $\Delta G_1^{\mathrm{np}}/k_{\mathrm{B}}T$, whereas the predominant contribution to $\Delta G_1/k_{\mathrm{B}}T$ arose from the electrostatic contribution $\Delta G_1^{\mathrm{elec}}/k_{\mathrm{B}}T$. The pressure effect by $\Delta G_1^{\mathrm{elec}}/k_{\mathrm{B}}T$ was important to the high-pressure denaturation of the protein, as discussed below.

Based on the pressure dependence of $\left(\Delta E_i^{\mathrm{eff}} / k_{\mathrm{B}} T \right)^*$, we found two different typical conformations whose appearance probabilities increased at higher pressures. One was compact, comparable to the native structure. Thus, the decrease in the electrostatic contribution $\left(\Delta\Delta G_i^{\mathrm{elec}} / k_{\mathrm{B}} T \right)^*$ with increasing pressure was not large because of the compact conformation with a small solvent-accessible surface area, while the increase in the nonpolar contribution $\left(\Delta\Delta G_i^{\mathrm{np}} / k_{\mathrm{B}} T \right)^*$ was sufficiently suppressed by the compactness of that conformation. The other had an expanded conformation with a large R_s. Thus, the decrease in the electrostatic contribution $\left(\Delta\Delta G_i^{\mathrm{elec}} / k_{\mathrm{B}} T \right)^*$ with the increase in pressure was significantly larger than that for the former because of the electrostatic interactions between the protein and water under the larger solvent-accessible surface area, although the increase in the nonpolar contribution $\left(\Delta\Delta G_i^{\mathrm{np}} / k_{\mathrm{B}} T \right)^*$ was larger than that for the former because of a larger excluded volume effect. The former—which can suppress the increase in $\left(\Delta\Delta G_i^{\mathrm{np}} / k_{\mathrm{B}} T \right)^*$—may relate to the sufficiently compact denatured conformation, proposed by Harano and Kinoshita as the typical conformation appearing at high pressures [71]. The latter—which is stabilized by the decrease in the electrostatic contribution $\left(\Delta\Delta G_i^{\mathrm{elec}} / k_{\mathrm{B}} T \right)^*$ caused by the large solvent-accessible surface area—is also important to high-pressure unfolding.

The mechanisms discussed in the present study on the high-temperature and high-pressure unfolding of chignolin require further investigation by extensive conformation ensembles and by determining the free energy landscape under various thermodynamic conditions. The RMDFT can be a powerful tool to perform efficient high-precision SFE calculations, since time-consuming 3D-RISM calculations of the solvent density distribution functions have already been sufficiently accelerated by progress in graphic processing units [72].

Keywords: Temperature and pressure dependences of solvation free energy, classical density functional theory, 3D-RISM theory, hydrophobic solute, protein, chignolin, thermal denaturation, high-pressure unfolding.

Additional Supporting Information may be found in the online version of this article.

References

[1]   M. P. Allen, D. J. Tildesley, *Computer Simulation of Liquids*, Oxford University Press, Oxford, **1989**.

[2]   D. Frenkel, B. Smit, *Understanding Molecular Simulation*, Academic Press, San Diego, **2001**.

[3]   W. L. Jorgensen, C. Ravimohan, *J. Chem. Phys.* **1985**, *83*, 3050–3054.

[4]   T. P. Straatsma, H. J. C. Berendsen, *J. Chem. Phys.* **1988**, *89*, 5876–5886.

[5]   M. R. Shirts, J. W. Pitera, W. C. Swope, V. S. Pande, *J. Chem. Phys.* **2003**, *119*, 5740.

[6]   M. R. Shirts, V. S. Pande, *J. Chem. Phys.* **2005**, *122*, 134508.

[7]   J. Tomasi, M. Persico, *Chem. Rev.* **1994**, *94*, 2027–2094.

[8]   C. J. Cramer, D. G. Truhlar, *Chem. Rev.* **1999**, *99*, 2161–2200.

[9]   J. Tomasi, B. Mennucci, R. Cammi, *Chem. Rev.* **2005**, *105*, 2999–3093.

[10]   A. C. Chamberlin, C. J. Cramer, D. G. Truhlar, *J. Phys. Chem. B* **2006**, *110*, 5665–5675.

[11]   A. C. Chamberlin, C. J. Cramer, D. G. Truhlar, *J. Phys. Chem. B* **2008**, *112*, 3024–3039.

[12]   K. Sato, H. Chuman, S. Ten-no, *J. Phys. Chem. B* **2005**, *109*, 17290–17295.

[13]   S. J. Singer, D. Chandler, *Mol. Phys.* **1985**, *55*, 621–625.

[14]   S. Ten-no, *J. Chem. Phys.* **2001**, *115*, 3724–3731.

[15]   A. Kovalenko, F. Hirata, *J. Chem. Phys.* **2000**, *113*, 2793.

[16]   E. L. Ratkova, G. N. Chuev, V. P. Sergiievskyi, M. V. Fedorov, *J. Phys. Chem. B* **2010**, *114*, 12068–12079.

[17]   J.-F. Truchon, B. M. Pettitt, P. Labute, *J. Chem. Theory Comput.* **2014**, *10*, 934–941.

[18]   D. S. Palmer, V. P. Sergiievskyi, F. Jensen, M. V. Fedorov, *J. Chem. Phys.* **2010**, *133*, 044104.

[19]   G. N. Chuev, M. V. Fedorov, J. Crain, *Chemical Physics Letters* **2007**, *448*, 198–202.

[20]   A. I. Frolov, E. L. Ratkova, D. S. Palmer, M. V. Fedorov, *J. Phys. Chem. B* **2011**, *115*, 6011–6022.

[21]   D. S. D. Palmer, A. I. A. Frolov, E. L. E. Ratkova, M. V. M. Fedorov, *Mol. Pharm.* **2011**, *8*, 1423–1429.

[22]   D. S. Palmer, A. I. Frolov, E. L. Ratkova, M. V. Fedorov, *J. Phys.: Condens. Matter* **2010**, *22*, 492101–492101.

[23]   M. Misin, M. V. Fedorov, D. S. Palmer, *J. Chem. Phys.* **2015**, *142*, 091105–091105.

[24]   V. P. Sergiievskyi, G. Jeanmairet, M. Levesque, D. Borgis, *J. Phys. Chem. Lett.* **2014**, *5*, 1935–1942.

[25]   Y. Liu, J. Fu, J. Wu, *J. Phys. Chem. Lett.* **2013**, *4*, 3687–3691.

[26]   Y. Liu, S. Zhao, J. Wu, *J. Chem. Theory Comput.* **2013**, *9*, 1896–1908.

[27]   S. Zhao, Z. Jin, J. Wu, *J. Phys. Chem. B* **2011**, *115*, 6971–6975.

[28]   N. Matubayasi, M. Nakahara, *J. Chem. Phys.* **2000**, *113*, 6070–6081.

[29]   N. Matubayasi, M. Nakahara, *J. Chem. Phys.* **2002**, *117*, 3605–3616.

[30]   N. Matubayasi, M. Nakahara, *J. Chem. Phys.* **2003**, *119*, 9686–9702.

[31]   Y. Karino, M. V. Fedorov, N. Matubayasi, *Chem. Phys. Lett.* **2010**, *496*, 351–355.

[32]   B. Guillot, Y. Guissani, *J. Chem. Phys.***1993**, *99*, 8075–8094.

[33]   T. Sumi, A. Mitsutake, Y. Maruyama, *J. Comput. Chem.* **2015**, *36*, 1359–1369.

[34]   T. Sumi, A. Mitsutake, Y. Maruyama, *J. Comput. Chem.* **2015**, *36*, 2009–2011.

[35]   D. Chandler, J. D. McCoy, S. J. Singer, *J. Chem. Phys.* **1986**, *85*, 5971.

[36]   D. Chandler, J. D. McCoy, S. J. Singer, *J. Chem. Phys.* **1986**, *85*, 5977.

[37]   J. P. Donley, J. G. Curro, J. D. McCoy, *J. Chem. Phys.* **1994**, *101*, 3205.

[38]   T. Sumi, T. Imai, F. Hirata, *J. Chem. Phys.* **2001**, *115*, 6653.

[39]   T. Sumi, F. Hirata, *J. Chem. Phys.* **2003**, *118*, 2431–2442.

[40]   J. K. Percus, *Phys. Rev. Lett.* **1962**, *8*, 462–463.

[41]   T. Miyata, J. Thapa, *Chem. Phys. Lett.* **2014**, *604*, 122–126.

[42]   T. Sumi, Y. Maruyama, A. Mitsutake, K. Koga, *J. Chem. Phys.* **2016**, *144*, 224104–224104.

[43]   H. C. Andersen, D. Chandler, *J. Chem. Phys.* **1972**, *57*, 1918–1929.

[44]   D. Chandler, H. C. Andersen, *J. Chem. Phys.* **1972**, *57*, 1930–1937.

[45]   F. Hirata, Ed., *Molecular Theory of Solvation*, Kluwer Academic Publishers, Dordrecht, **2003**.

[46]   W. L. Jorgensen, J. Chandrasekhar, J. D. Madura, R. W. Impey, M. L. Klein, *J. Chem. Phys.* **1983**, *79*, 926.

[47]   H. Berendsen, J. R. Grigera, T. P. Straatsma, *J. Phys. Chem.* **1987**, *91*, 6269–6271.

[48]   Y. Rosenfeld, *Phys. Rev. Lett.* **1989**, *63*, 980–983.

[49]   R. Roth, R. Evans, A. Lang, G. Kahl, *J. Phys.: Condens. Matter* **2002**, *14*, 12063–12078.

[50]   Y.-X. Yu, J. Wu, *J. Chem. Phys.* **2002**, *117*, 10156.

[51]   T. Sumi, H. Sekino, *J. Phys. Soc. Jpn.* **2008**, *77*, 034605.

[52]   A. Kovalenko, F. Hirata, *J. Chem. Phys.* **1999**, *110*, 10095–10112.

[53]   B. M. Pettitt, *J. Chem. Phys.* **1982**, *77*, 1451.

[54]   H. S. Ashbaugh, N. J. Collett, H. W. Hatch, J. A. Staton, *J. Chem. Phys.* **2010**, *132*, 124504–124504.

[55]   T. Sumi, H. Sekino, *Phys. Chem. Chem. Phys.* **2011**, *13*, 15829–15832.

[56]   T. Sumi, H. Sekino, *RSC Adv.* **2013**, *3*, 12743.

[57]   D. Paschek, *J. Chem. Phys.* **2004**, *120*, 6674–6690.

[58]   J. Z. Vilseck, J. Tirado-Rives, W. L. Jorgensen, *Phys. Chem. Chem. Phys.* **2015**, *17*, 8407–8415.

[59]   S. Honda, K. Yamasaki, Y. Sawada, H. Morii, *Struct./Fold. Des.* **2003**, *12*, 1507–1518.

[60]   P. Kührová, A. De Simone, M. Otyepka, R. B. Best, *Biophys. J.* **2012**, *102*, 1897–1906.

[61]   A. Mitsutake, H. Takano, *J. Chem. Phys.* **2015**, *143*, 124111–124111.

[62]   D. Satoh, K. Shimizu, S. Nakamura, T. Terada, *FEBS Lett* **2006**, *580*, 3422–3426.

[63]   A. Suenaga, T. Narumi, N. Futatsugi, R. Yanai, Y. Ohno, N. Okimoto, M. Taiji, *Chem. Asian J.* **2007**, *2*, 591–598.

[64]   R. Harada, A. Kitao, *J. Phys. Chem. B* **2011**, *115*, 8806–8812.

[65]   M. S. Moghaddam, H. S. Chan, *J. Chem. Phys.* **2007**, *126*, 114507–114507.

[66]   Y. Maruyama, Y. Harano, *Chem. Phys. Lett.* **2013**, *581*, 85–90.

[67]   K. Koga, *Phys. Chem. Chem. Phys.* **2011**, *13*, 19749–19758.

[68]   C. M. Dobson, A. Šali, M. Karplus, *Angew. Chem. Int. Ed.* **1998**, *37*, 868–893.

[69]   S. Yasuda, T. Hayashi, M. Kinoshita, *J. Chem. Phys.* **2014**, *141*, 105103–105103.

[70]   K. Koga, *J. Phys. Chem. B* **2013**, *117*, 12619–12624.

[71]   Y. Harano, M. Kinoshita, *J. Chem. Phys.* **2006**, *125*, 24910–024910.

[72]   Y. Maruyama, F. Hirata, *J. Chem. Theory Comput.* **2012**, *8*, 3015–3021.